



# Bifurcation and scaling at the aging transition boundary in globally coupled excitable and oscillatory units

メタデータ	言語: eng 出版者: 公開日: 2018-02-06 キーワード (Ja): キーワード (En): 作成者: Daido, Hiroaki, Nishio, Kazuho メールアドレス: 所属:
URL	<a href="http://hdl.handle.net/10466/15726">http://hdl.handle.net/10466/15726</a>

## Bifurcation and scaling at the aging transition boundary in globally coupled excitable and oscillatory units

Hiroaki Daido\* and Kazuho Nishio†

*Department of Mathematical Sciences, Graduate School of Engineering, Osaka Prefecture University, Sakai 599-8531, Japan*

(Received 2 March 2016; published 26 May 2016)

Following a previous paper [Phys. Rev. E **88**, 052907 (2013)], we study in detail the mechanism of aging transition in globally and diffusively coupled excitable and oscillatory units. Here two of the three models taken up in the earlier work are used, each composed of a large number of units with their bifurcation parameters forming a uniform distribution. The control parameters are the coupling strength and the average of the bifurcation parameters. The present work is mostly devoted to a region of the phase diagram near the aging transition boundary with the coupling strength greater than its critical value for the onset of bistability and hysteresis. The bifurcation structure of each system at the aging transition boundary is investigated theoretically as well as numerically. Moreover, we show that critical scaling laws of order parameters  $S$  and  $M$  used in the previous paper are different depending on which region of the coupling strength to be chosen.

DOI: [10.1103/PhysRevE.93.052226](https://doi.org/10.1103/PhysRevE.93.052226)

### I. INTRODUCTION

Large-scale coupled oscillators appear in a variety of areas in science and technology and have been contributing greatly to the developments of those areas [1–5]. Although there are quite a few achievements in both theory and experiment concerning the dynamics of such systems [6,7], there are not so many studies about the robustness of their dynamic activity against the deterioration of constituent oscillators [8–17]. Such a study started nearly a decade ago, in which the concept of “aging,” defined as an increase in the ratio of inactive oscillators (i.e., damped oscillators in a generalized sense) in the system, was proposed and led to a discovery of an *aging transition*, namely, a transition from a dynamic state to a static one caused by the aging [8]. The critical ratio of inactive elements at which an aging transition takes place can be used as a measure of the robustness of the system’s dynamic activity against the deterioration of elements [8]. This quantity has also been used in the study of complex networks (see, e.g., [18–20]). There are many possible applications of the numerical and theoretical studies on the effects of aging defined above. One example is to develop *biological* pacemakers which can be created by revitalizing nonoscillatory heart pacemaker cells through a molecularbiological technique, in which the information of the critical ratio of inactive cells is crucial in order to recover the dynamic activity of the heart pacemaker [14,21]. Another example is found in the area of robotics, because any robot is driven by an artificial central pattern generator (CPG) [22,23], i.e., a system of coupled oscillators, and its robustness against the deterioration of its components is therefore of vital importance in maintaining the activity of the CPG. Moreover, it is reported that for those who suffer from Parkinson’s disease, the median frequency of the electroencephalogram (EEG) is lower than that of normal people [24], which fact might be due to an increase in the ratio of nonoscillatory neurons. A

possible reason is that, as shown below, the system’s period, reflected by a mean field, lengthens as it approaches the aging transition boundary in the course of aging, provided that the coupling strength is larger than a critical value to appear as  $K_f$  below. The dynamic activity, especially synchronization, plays an important role in neural systems [25], as well as many other disciplines, and hence it is indispensable to extensively investigate the robustness of the dynamic activity of coupled oscillators against the aging.

The aim of the present paper is to explore a region near the aging transition boundary that is left untouched in a previous paper dealing with globally coupled excitable and oscillatory units [26] and also to elucidate scaling laws of order parameters at that boundary in such a system. In the next paragraph, the content of the previous work is explained and then, in the following paragraph, the purpose of this work as well as main results are clearly stated.

In the previous paper [26] we discussed the behavior of large heterogeneous ensembles of globally and diffusively coupled units, each obeying the saddle-node bifurcation on an invariant circle (SNIC) scenario to exhibit either excitability or oscillation depending on its bifurcation parameter. The heterogeneity means the distribution of the bifurcation parameter within the ensemble, which is set to be a uniform distribution in the paper (see Ref. [14] for the case of a two-value distribution in the same context, which was published earlier). If the support of the distribution includes the saddle-node bifurcation point, then decreasing its average causes the ratio of inactive elements to increase, eventually leading to an aging transition [12,13]. The previous paper is concerned with three different ensembles whose units are phase oscillators, Morris-Lecar systems [27], and simplified oscillators, where the last one corresponds to the normal form of saddle-node bifurcation. The main purpose of the previous paper is to examine the effect of aging following earlier studies done for the case of the Hopf scenario [8–11]. A common feature of the three ensembles is that the  $(K, \mu_{av})$  phase diagram, where  $K$  and  $\mu_{av}$  are, respectively, the coupling strength and the average value of the bifurcation parameters in each ensemble, consists of three regions: static phase (SP), dynamic phase I (DP1), and dynamic phase II

\*Corresponding author: daido@ms.osakafu-u.ac.jp

†Present address: Meitec Corporation, Osaka Engineering Center, Nakazaki Nishi 2-4-12, Kita-Ku, Osaka 530-0015, Japan.

(DP2). The difference between DP1 and DP2 is whether the mean field is asymptotically constant (DP1) or not (DP2). Another common feature is the appearance of bistability and hysteresis at or near the aging transition boundary when the coupling strength reaches a threshold value,  $K_{oc}$ . In two of the ensembles mentioned above (phase and simplified oscillators) with  $K = K_{oc}$ , the ratio of oscillating components to the system size grows from zero, following a fractional power law with an exponent of  $2/3$  when the system exceeds the aging transition boundary from SP. The main focus here is on the region  $0 \leq K \leq K_{oc}$ .

The purpose of the present work is to elucidate the bifurcation structure related to the aging transition in the region  $K > K_{oc}$  and to clarify the critical behaviors of order parameters  $S$  and  $M$  (see below for details) at the aging transition boundary in a whole range of  $K$ . Here we only consider two of the three populations mentioned above, i.e., the one composed of phase oscillators and the other formed by simplified ones. There are two main results of the present work: One is the finding of a branching of dynamic solutions belonging to DP2 at a critical value of  $K$  that creates a new dynamic branch, hereafter referred to as a *floating branch*, and the other is the observation that the critical exponents of  $S$  and  $M$  discontinuously change as  $K$  is increased. These results are explained either analytically or based on numerical observations.

The paper is organized as follows. Section II is devoted to a description of the models and the order parameters mentioned above. Then, in Sec. III, numerical results are presented and a self-consistent theory is developed for each model to explain those simulation results. Section IV is concerned with scaling behaviors of the order parameters. Finally, in Sec. V, the paper is summarized with some remaining subjects stated. In the Appendix, theoretical expressions of a macroscopic quantity are presented for the ensemble of simplified oscillators. Numerical simulations were performed by means of the fourth order Runge-Kutta method with a time step of 0.01.

## II. MODELS AND ORDER PARAMETERS

The model systems employed in the present work are displayed below:

(1) First is the phase oscillator model [12,26,28],

$$\frac{d\theta_j}{dt} = a_j - \sin \theta_j + \frac{K}{N} \sum_{i=1}^N \sin(\theta_i - \theta_j), \quad (1)$$

for  $1 \leq j \leq N$ , where  $\theta_j$  and  $a_j$  are the phase and the bifurcation parameter of the  $j$ th oscillator. The latter is set as

$$a_j = a_{av} - \gamma + 2 \frac{j-1}{N-1} \gamma, \quad (2)$$

where  $a_{av}$  is the mean value of all  $a_j$  and  $\gamma > 0$  is the half-width of the uniform distribution. Because of a symmetry of this model, only the region  $a_{av} > 0$  is treated below.

(2) Second is the simplified oscillator model [26],

$$\frac{dx_j}{dt} = \mu_j + x_j^2 + \frac{K}{N} \sum_{i=1}^N (x_i - x_j), \quad (3)$$

for  $1 \leq j \leq N$ , where  $x_j$  is restricted in the range  $-1 \leq x \leq 1$ ; if  $x_j(t) = 1$ , then  $x_j(t+0)$  is reset to  $-1$ . To simulate the evolution of this model, after each step of numerical integration, the new values of  $x_j$  ( $1 \leq j \leq N$ ) are examined and if some of them are larger than or equal to 1, then they are all reset to  $-1$  and this process is repeated, where it is taken into account that the time step 0.01 is small [29]. The bifurcation parameters  $\mu_j$  are given in the same way as for system (1):

$$\mu_j = \mu_{av} - \gamma + 2 \frac{j-1}{N-1} \gamma. \quad (4)$$

For this model, we consider the case  $K < 2$ , because, otherwise, the saddle-node bifurcation does not occur in any unit.

The order parameters  $S$  [12,26] and  $M$  [8,26,30,31] are defined as

$$S = \left( N^{-1} \sum_{j=1}^N \langle |\mathbf{x}_j - \langle \mathbf{x}_j \rangle|^2 \rangle \right)^{1/2}, \quad (5)$$

$$M = \langle |\mathbf{X} - \langle \mathbf{X} \rangle|^2 \rangle^{1/2}, \quad (6)$$

where  $\mathbf{x}_j$  stands for the state vector of the  $j$ th unit,  $\mathbf{X} \equiv \sum_{j=1}^N \mathbf{x}_j / N$  is the mean-field, and the brackets stand for a time average. The third order parameter,  $R$ , is the ratio of oscillating units to the system size  $N$  in an ensemble [26]. The order parameter  $S$  is used to detect the nonstationarity of the system, while the order parameter  $M$  works to distinguish the dynamic phases: DP1 ( $M = 0$ ) and DP2 ( $M > 0$ ). The units of systems (1) and (3) are all one-dimensional and hence  $\mathbf{x}_j$  and  $\mathbf{X}$  are replaced with  $x_j$  and  $X$ , respectively, in model (3), while in model (1), we use  $e^{i\theta_j}$  as  $x_j$  and

$$Z = \frac{1}{N} \sum_{j=1}^N e^{i\theta_j} \quad (i = \sqrt{-1}) \quad (7)$$

as the mean field [3]. Of course, the order parameter  $R$  is zero in SP and nonvanishing in either of the two dynamic phases. The criteria for identifying SP, DP1, and DP2 are specified in the captions of phase diagrams to appear below.

## III. NUMERICAL RESULTS AND THEORY

In this section, we describe results of numerical simulations and explain some of them theoretically on the basis of a self-consistent analysis for each model.

### A. Phase oscillator model

A global  $(K, a_{av})$  phase diagram is given in Fig. 1(a), which is the same as Fig. 3(a) of the previous paper [26], except for the theoretical boundary where  $R$  vanishes. Figure 1(b) shows a region just beyond  $K = K_{oc} \sim 0.9$  with four boundaries found by simulation. Boundary A is where the system makes a transition from SP to DP1 or DP2 for increasing  $a_{av}$  with relayed initial conditions (see the caption of Fig. 1). Boundary B is where a reverse transition occurs from DP1 to SP for decreasing  $a_{av}$  with initial conditions taken the same way. The other two boundaries separate DP1 and DP2, which have



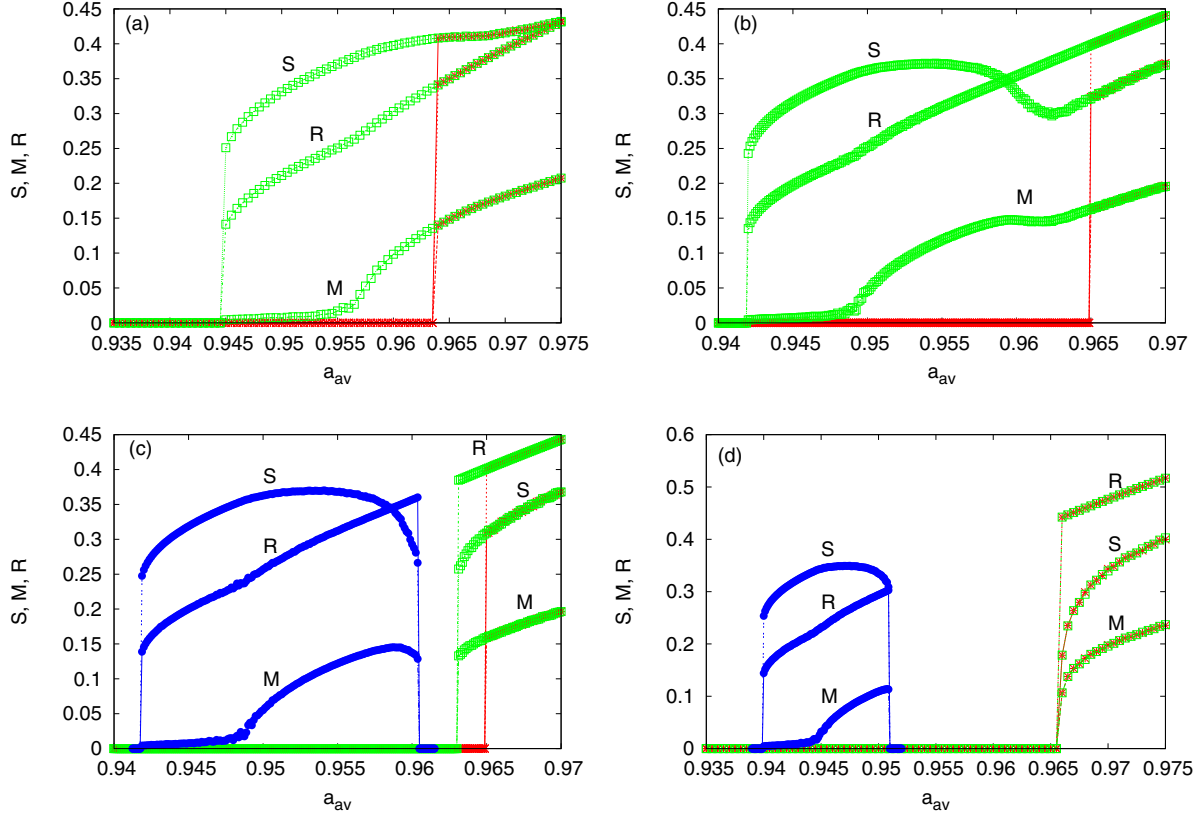


FIG. 3. Behaviors of the order parameters  $S$ ,  $M$ , and  $R$  in the phase-oscillator model ( $\gamma = 0.5$ ,  $N = 6400$ ). Relayed initial conditions are used (see the caption of Fig. 1). The data displayed (asterisks, red; squares, green) are those for increasing and decreasing  $a_{av}$ , respectively, while solid circles (blue) show the floating branch with its neighborhoods included. The vertical lines in each panel show where discontinuous transitions take place, except for the rightmost vertical line of panel (d). (a)  $K = 1.13$ ; (b)  $K = 1.148$  (immediately before  $K = K_f$ ); (c)  $K = 1.149$  (immediately after  $K = K_f$ ); (d)  $K = 1.16$  ( $> K_h$ ). The floating branches in (c) and (d) were found using the final values of all variables around a roughly middle point of the same branch for a previous value of  $K$  as the initial condition.

where

$$F_1(A, a_{av}) \equiv \frac{\pi}{2} - \sin^{-1} u - u\sqrt{1-u^2}, \quad (12)$$

with  $u \equiv (a_{av} - \gamma)/A$ , and

$$F_2(A, a_{av}) \equiv \frac{4\gamma a_{av}}{A^2} - v\sqrt{v^2-1} + \ln(v + \sqrt{v^2-1}), \quad (13)$$

where  $v \equiv (a_{av} + \gamma)/A$ . Referring to Eq. (9), we find a self-consistent equation to determine both  $A$  and  $\beta$ :

$$Ae^{i\beta} = \frac{1}{1 - \frac{K}{4\gamma}\{F_1(A, a_{av}) + iF_2(A, a_{av})\}}. \quad (14)$$

An equation of  $A$  follows from the last equation by taking the modulus of both of its sides. Then  $\beta$  is fixed by Eq. (14) with a solution of  $A$ 's equation inserted. Let  $a_c$  denote the critical value of  $a_{av}$  at which the system makes a transition from SP to DP1. Noting that  $A = a_c + \gamma$  there, we obtain an equation of  $a_c$  as follows:

$$a_c + \gamma = \frac{1}{\sqrt{\left\{1 - \frac{K}{4\gamma}F_1(a_c + \gamma, a_c)\right\}^2 + \left\{\frac{K}{4\gamma}F_2(a_c + \gamma, a_c)\right\}^2}}. \quad (15)$$

For  $K = K_{oc}$ , the bifurcation of a solution belonging to DP1 changes its character from normal to inverted [26], so that the

critical value of  $K$  is determined by the condition

$$1/\left(\frac{dR}{da_{av}}\right)_{a_c} = 0. \quad (16)$$

By numerically solving Eqs. (15) and (16), we have found

$$K_{oc} = 0.9035971\dots \quad (17)$$

and also  $a_c = 0.9385988\dots$  for  $K = K_{oc}$ . The theoretical boundary  $a_{av} = a_c$  obtained from Eq. (15) is shown in Fig. 1(a), agreeing with the aging transition boundary found by simulation. However, this is only the case with the region  $K \leq K_{oc}$ . The discrepancy between both of them appears for  $K > K_{oc}$ , becoming more and more serious as  $K$  grows in that region. Figure 4(b) gives clearer evidence for the disagreement for large  $K$  in the form of a bifurcation diagram. This point is addressed later. The order parameter  $S$  can be calculated as follows:

$$\begin{aligned} S &= \sqrt{1 - \frac{1}{N} \sum_{j=1}^N |e^{i\theta_j}|^2} \\ &= \sqrt{1 + \frac{a_{av} - \gamma}{2\gamma} - \frac{A}{2\gamma} \left\{ I(v) + \frac{4}{3} \right\}}, \end{aligned} \quad (18)$$

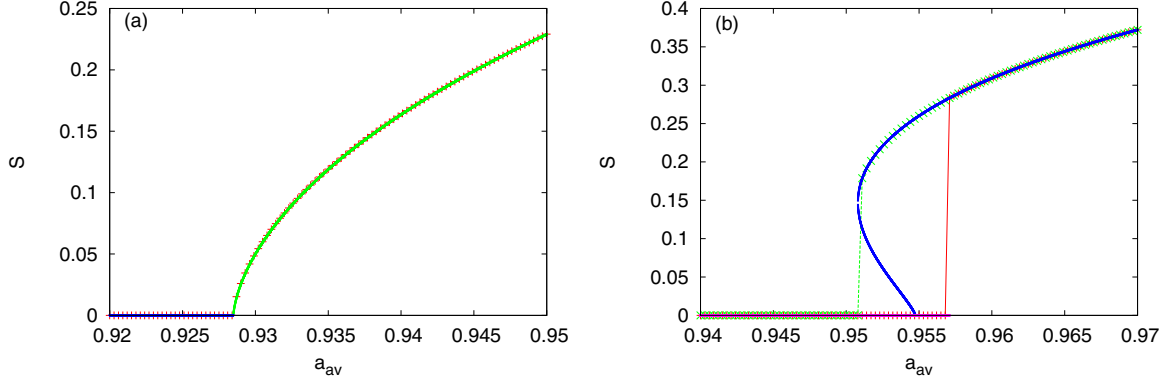


FIG. 4. Critical behavior of the order parameter  $S$  in the phase-oscillator model ( $\gamma = 0.5$ ,  $N = 6400$ ). (a)  $K = 0.85$  ( $< K_{oc}$ ). The symbols (+, red) are simulation results. The curves (blue, green) are due to theory. (b)  $K = 1.05$  ( $> K_{oc}$ ). The curves (magenta, blue) are due to theory. Panel (b) displays the simulation data obtained for changing  $a_{av}$  with relayed initial conditions (upward, +, red; downward,  $\times$ , green) (see the caption of Fig. 1). See the point at which the lower theoretical curve with  $S > 0$  (blue) intersects the horizontal axis, whose abscissa is  $a_c$ . The right (red) and left (green) vertical lines correspond to boundaries A and B, respectively, in Fig. 1(b).

where

$$I(x) \equiv \frac{2}{3}x^3 - x - \frac{2}{3}(x^2 - 1)^{\frac{3}{2}}. \quad (19)$$

Similarly, the self-consistent equation of  $A$  can be derived in other cases as well. For the case  $A > a_{av} + \gamma$ , all units are stationary. By way of Eq. (8), we obtain

$$Ae^{i\beta} \left\{ 1 - \frac{K}{4\gamma}(G_1 + iG_2) \right\} = 1 \quad (20)$$

and

$$Z = \frac{G_1 + iG_2}{4\gamma - K(G_1 + iG_2)}, \quad (21)$$

where

$$\begin{aligned} G_1 &\equiv \sin^{-1} v - \sin^{-1} u + v\sqrt{1-v^2} - u\sqrt{1-u^2}, \\ G_2 &\equiv v^2 - u^2, \end{aligned} \quad (22)$$

with  $u$  and  $v$  introduced above. In this case,  $S = M = R = 0$ .

For the case  $0 < A < a_{av} - \gamma$ , all units are oscillators and hence  $R = 1$ . It is possible to obtain the results

$$Ae^{i\beta} \left[ 1 - \frac{K}{2i\gamma} \{h(v) - h(u)\} \right] = 1 \quad (23)$$

and

$$Z = \frac{h(v) - h(u)}{2i\gamma - K\{h(v) - h(u)\}}, \quad (24)$$

where

$$h(x) \equiv \frac{1}{2}(x\sqrt{x^2-1} - \ln|x + \sqrt{x^2-1}| - x^2). \quad (25)$$

The order parameter  $S$  is given by

$$S = \sqrt{1 - \frac{A}{2\gamma} \{I(v) - I(u)\}}, \quad (26)$$

with  $I(x)$  defined earlier.

Let us now make a comparison between theory and simulation. In Fig. 1(a), a theoretical boundary is drawn on which the order parameter  $R$  vanishes. A nice agreement is found with the boundary obtained by simulation for  $K \leq K_{oc}$ ,

which is because the supercritical side lies in DP1 and hence the above theory is applicable. This is also the case with Fig. 2, in which the two black boundaries, due to theory, agree with simulation results. We can also confirm the validity of theory in Figs. 5 and 6, where the behaviors of  $S$  and  $|Z|$  are displayed. It should be noted, however, that the theory developed above is only applicable to SP and DP1. The reason why the theoretical  $a_c$  shifts downward from the boundary between SP and DP for  $K > K_{oc}$  [see Fig. 1(a)] is obvious from Fig. 5, which shows bifurcation diagrams of  $|Z|$  for both  $K < K_{oc}$  and  $K > K_{oc}$ . It is found in Fig. 5(b) that for  $K > K_{oc}$ , the branch of  $R = 0$  extends beyond  $a_{av} = a_c$  to a point, say,  $a_{av} = a_J$  where it turns back, eventually meeting another branch with  $R > 0$  at  $a = a_c$ . The middle curve in the bistable region, composed of these two branches which merge at  $a_{av} = a_c$ , is expected to be unstable and therefore  $a_{av} = a_c$  deviates downward from the jumping point  $a_{av} = a_J$  encountered as  $a_{av}$  is varied upward with relayed initial conditions. This result is consistent with Fig. 4 (b), where the stable and unstable branches with  $R = 0$  in the region of  $a_c < a_{av} < a_J$  perfectly overlap because of  $S = 0$  in either branch.

Let us now consider the mechanism of the appearance of the floating branch. Figure 6 displays a couple of bifurcation diagrams and also  $Z$ 's behaviors on the complex plane. Figure 6(a), which is a bifurcation diagram just after  $K = K_f$ , indicates that there is an interval of  $a_{av}$  in which no DP2 solutions exist. Namely, at both ends of the interval, discontinuous transitions occur from DP2 to SP. As  $K$  grows, this interval expands and eventually at  $K = K_h$  its right end reaches the point where the saddle-node bifurcation of SP solutions takes place and this situation remains the same for  $K > K_h$  [see Fig. 6(b)]. On the other hand, what happens at the lower end of the floating branch is also a discontinuous transition from DP1 to SP due to the saddle-node bifurcation of DP1 solutions. Then what is the mechanism of the discontinuous transitions from DP2 to SP? Figures 6(c) and 6(d) give a hint to it: Comparing both panels makes us realize that as the system approaches the discontinuous transition point from above, the unstable fixed point (SP) becomes closer and closer to the orbit of  $Z$ . Hence, the discontinuous transition is expected to happen

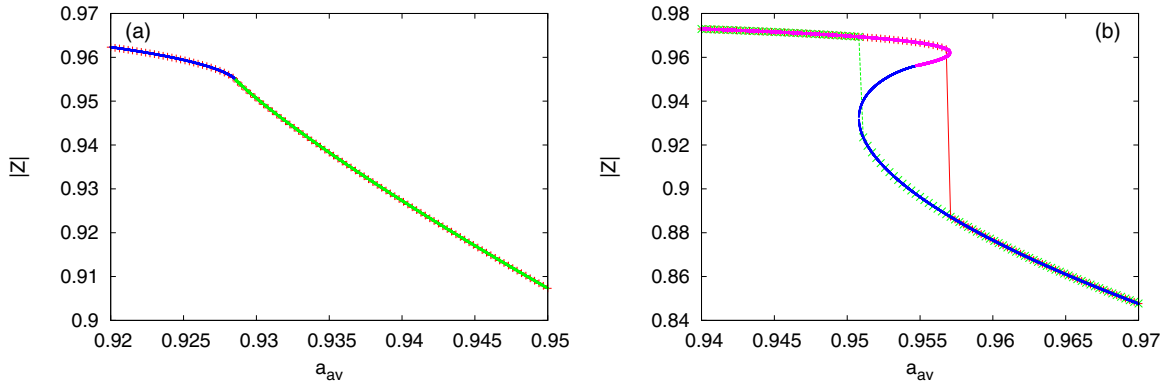


FIG. 5. Behavior of  $|Z|$  in the phase oscillator model ( $\gamma = 0.5$ ,  $N = 6400$ ), where the simulation data show the moduli of time averages of  $Z$ . (a)  $K = 0.85 (< K_{oc})$ . The simulation results: +, red. The curves are theoretical: the left one (blue) and the right one (green) are subcritical ( $R = 0$ ) and supercritical ( $R > 0$ ) branches, respectively. (b)  $K = 1.05 (> K_{oc})$ . The simulation results are obtained by increasing (+, red) and decreasing ( $\times$ , green)  $a_{av}$  with relayed initial conditions (see the caption of Fig. 1). The curves are theoretical: the magenta (mostly on the left side) and the blue one (mostly on the right side) correspond to the branches of  $R = 0$  and  $R > 0$ , respectively.

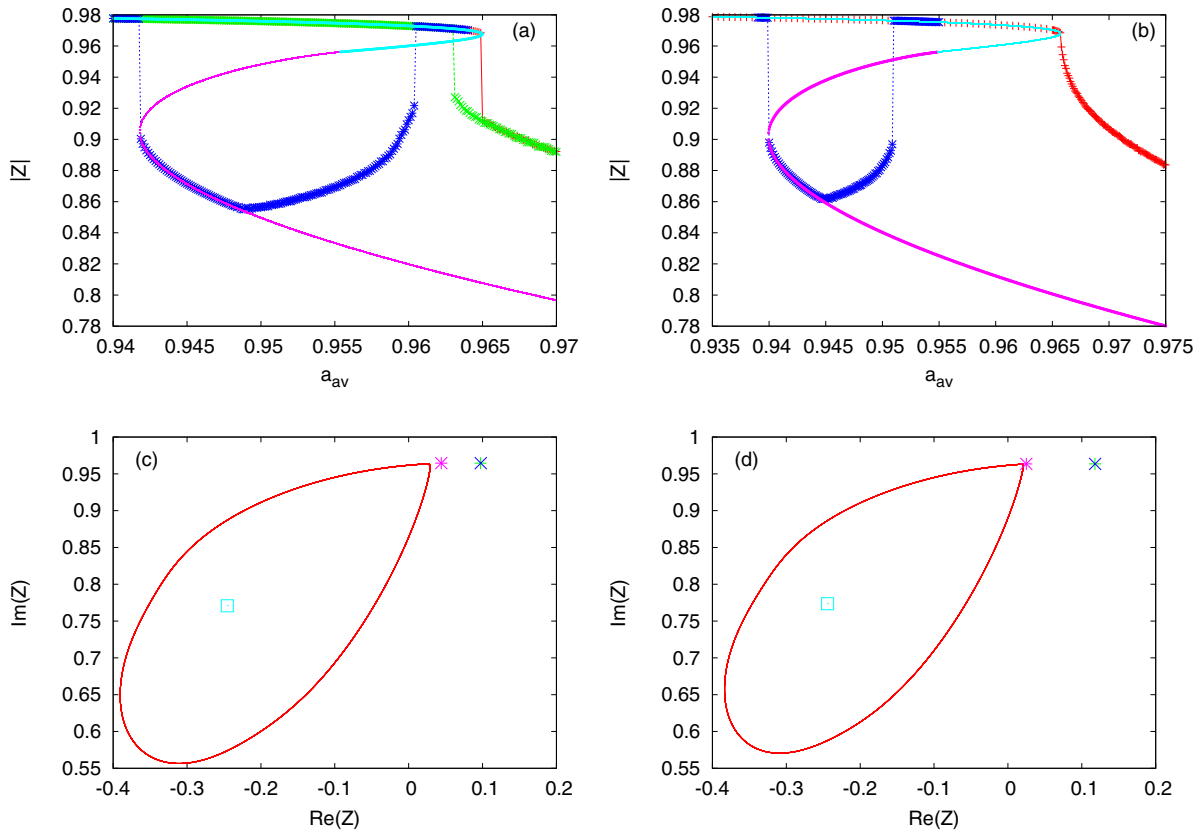


FIG. 6. Mechanism of the branching of dynamic solutions corresponding to DP2 in the phase-oscillator model ( $\gamma = 0.5$ ,  $N = 6400$ ), where the ordinate is  $|Z|$ . Simulation results have been obtained using relayed initial conditions (see the caption of Fig. 1). The simulation data in panels (a) and (b) are the moduli of  $Z$ 's time averages. (a)  $K = 1.149$  (immediately after  $K = K_f$ ). Simulation results: data for increasing  $a_{av}$  (+, red) and for decreasing  $a_{av}$  ( $\times$ , green) and the floating branch with its neighborhoods included (asterisk, blue). The curves are due to theory: The upper cyan and lower magenta curves correspond to SP and DP1, respectively. The discontinuous transitions from DP2 to SP occur at  $a_{av} \sim 0.9604$  and  $\sim 0.9631$ . (b)  $K = 1.16 (> K_h)$ . Simulation results: data for increasing  $a_{av}$  (+, red) and the floating branch with its neighborhoods included (asterisk, blue). The curves are due to theory: The upper cyan and lower magenta curves correspond to SP and DP1, respectively. Note that in each of the above two panels, the point at which the floating branch deviates from the theoretical DP1 branch divides the former branch into DP1 and DP2. (c) Behavior of  $Z$  on the complex plane:  $K = 1.149$ ,  $a_{av} = 0.9645$ . Simulation results: the closed curve (red, DP2) and the point (+, green, SP). Theory: three points ( $\times$ , blue, SP, stable), (asterisk, magenta, SP, unstable), and (square, cyan, DP1, unstable). (d) Behavior of  $Z$  on the complex plane:  $K = 1.149$ ,  $a_{av} = 0.9635$ . Details are the same as panel (c).

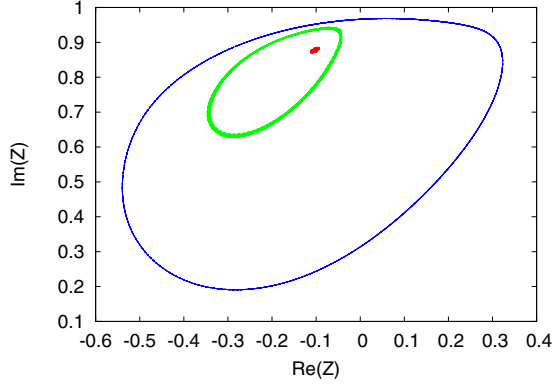


FIG. 7. Trajectories of  $Z$  on the complex plane obtained from the phase-oscillator model ( $\gamma = 0.5$ ,  $N = 6400$ ). The smallest (red), middle (green), and largest (blue) “closed” curves are for  $(K, a_{av}) = (1.05, 0.958)$ ,  $(1.13, 0.965)$ , and  $(1.2, 0.97)$ , respectively.

because of their collision with the disappearance of the orbit after that. This same scenario has been confirmed for the left end of the interval with no DP2 solutions (data not shown). It has also been confirmed that the period of the closed orbit on the complex plane becomes larger as the system moves closer to each transition point, which is consistent with the above scenario. As the coupling strength  $K$  approaches  $K_f$  from above, that interval should become smaller and vanish at  $K = K_f$ . However, although this scenario seems plausible, it has yet to be supported by developing a theory to cover the region of DP2.

Before going on to the next section, let us see how the mean-field  $Z$  behaves on the complex plane as the time  $t$  increases. Here we concentrate on its behavior at three points in the phase diagram shown in Fig. 1(b), which are located just beyond the aging transition boundary with label A. Figure 7 shows the orbits of  $Z$  at those points. The smallest one there comes from a point belonging to DP1, whereas the other two correspond to the rest of the points that are located in DP2. The smallest orbit in the figure is generated by finite-size fluctuations and hence of the minimum size. Moreover, in DP2, the size of the orbit grows with  $K$ , as confirmed in Fig. 7. These results are consistent with the definitions of DP1 and DP2. Figure 8 displays the pattern of all average frequencies for each of the three points used in Fig. 7, where the average frequency of the  $j$ th unit means the time average of  $\dot{\theta}_j$ , i.e.,  $\langle \dot{\theta}_j \rangle$ . No frequency synchronization can be found among the oscillating units for the point in DP1, but for the rest of the points, there exist two clusters of frequency synchronization and for the point with the largest  $K$ , the larger cluster overwhelms the other. This is the reason why the thickness of the middle-size orbit is much larger than that of the largest one, as seen in Fig. 7.

### B. Simplified oscillator model

In this section, we study the behavior of the simplified oscillator model, as displayed in Eq. (3) [26]. This is to confirm the generality of the findings reported in the foregoing section for the phase-oscillator model. Each unit of the present model, although simple, plays a significant role in nonlinear dynamics as the normal form of the saddle-node bifurcation [32]. Hence,

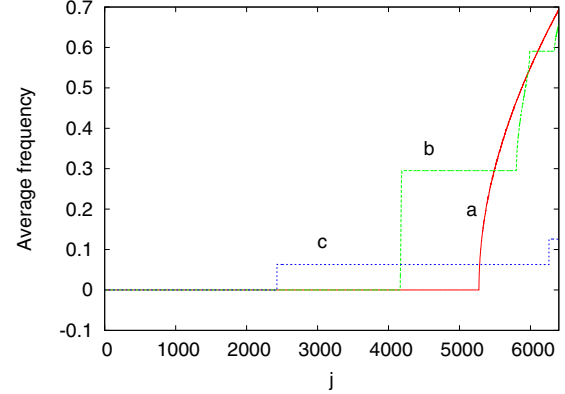


FIG. 8. Average frequency vs  $j$  for the phase oscillator model ( $\gamma = 0.5$ ,  $N = 6400$ ). The parameters  $K$  and  $a_{av}$  of the data labeled “a”, “b”, and “c” are the same as those of the smallest, middle, and largest “curves” in Fig. 7, respectively.

if the present system exhibits qualitatively the same behavior as the previous one, its generality should be guaranteed. As described below, this is actually the case.

Figure 9 presents global and local phase diagrams of the simplified oscillator model. It is already reported in Ref. [26] that the global one, Fig. 9(a), is similar to that of the phase-oscillator model, Fig. 1(a). We also see that its local structure near  $K = K_{oc}$  shown in Fig. 9(b) is qualitatively the same as that in Fig. 1(b). There are two more common features of the two models in terms of the phase diagram: One is the disagreement between the theoretical and numerical aging transition boundaries on which  $R$  is zero for  $K > K_{oc}$ , as noticed in Fig. 9(a), and the other is the appearance of the floating branch, as shown in Fig. 10. The latter is also confirmed by checking out the behaviors of the order parameters in Fig. 11. As to the discrepancy between the two boundaries, the reason is just the same as in the case of the phase-oscillator model (see Fig. 12). Figure 13 is evidence that the branching of dynamic solutions belonging to DP2 takes place in the same way as in the phase-oscillator model: Panel (a) is similar to Figs. 6(a) and 6(b) demonstrates that the discontinuous transition from DP2 to SP at the right end of the floating branch is caused by a collision between the orbit and an unstable fixed point belonging to DP1. This scenario has also been numerically confirmed to apply to the similar transition at the left end of the hysteresis region, in which the orbit collides with the unstable SP fixed point (data not shown). In Fig. 14, the time series data of  $X$  are shown for three points located just beyond the boundary with label A in Fig. 9(b); one of them lies in DP1 (the data with almost no variation), while the rest belong to DP2. All average frequencies in the population are plotted against unit number  $j$  in Fig. 15, which have been computed at the same points in the phase diagram. What we can learn from these two figures is the same as what Figs. 7 and 8 reveal.

A self-consistent theory for the simplified oscillator model is already developed in the previous paper [26], but it is only for the purpose of studying the behavior of the order parameter  $R$ . Here the theory is extended to explain the behaviors of the other order parameters in SP and DP1. Part of the results displayed

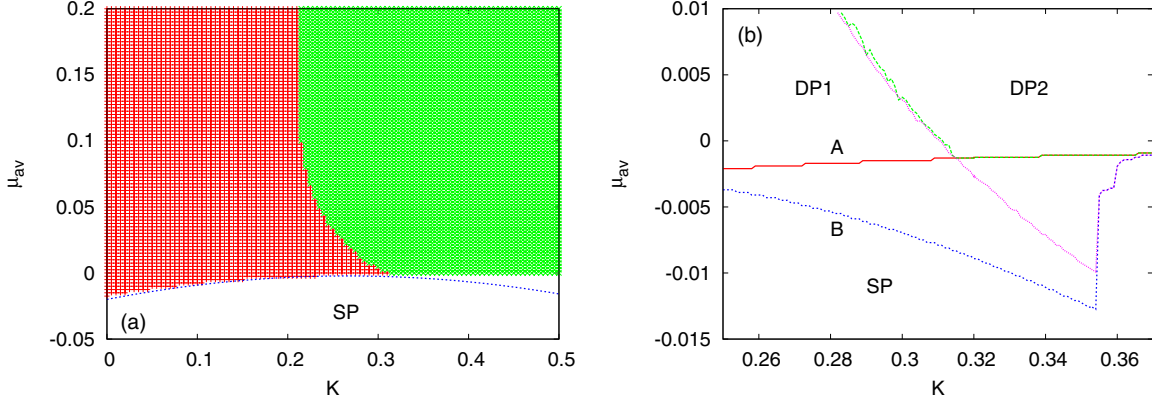


FIG. 9. Phase diagrams of the simplified oscillator model, Eq. (3). (a)  $\gamma = 0.02$ ,  $N = 1000$ : DP1 (upper left side, red), DP2 (upper right side, green) [26]. The broken curve (blue) is a theoretical boundary at which the order parameter  $R$  vanishes. (b)  $\gamma = 0.02$ ,  $N = 4000$ : Relayed initial conditions are used (see the caption of Fig. 1). The meanings of the line styles (colors) and the labels are the same as in Fig. 1(b). The boundaries A and B are drawn using the criterion that the system is in DP if  $S > 0.02$ . Moreover, the boundaries separating DP1 and DP2 are determined by the same criterion: The system is in DP2 if  $M > 0.02$ . Note that the value 0.02 is not very different from  $\sqrt{1/N}$  ( $\approx 0.0158 \dots$  for  $N = 4000$ ) used in drawing panel (a) [26].

below already appears in the same paper. The system size  $N$  is assumed to be infinity. Moreover, only the case  $\mu_{av} > \gamma$  is considered in what follows.

First of all, it should be noticed that a unit with  $\mu_j$  larger than  $\mu^*$  oscillates, while it does not oscillate otherwise, where

$$\mu^* \equiv \frac{K^2}{4} - KX. \quad (27)$$

It is then possible to construct a self-consistent equation of  $X$  for three different cases. For the case  $\mu_{av} - \gamma \leq \mu^* \leq \mu_{av} + \gamma$ , the equation of  $X$  reads

$$X = \frac{1}{2\gamma} \int_{\mu_{av}-\gamma}^{\mu^*} d\mu \left( \frac{K}{2} - \sqrt{\mu^* - \mu} \right) + \frac{1}{2\gamma} \int_{\mu^*}^{\mu_{av}+\gamma} d\mu \left\{ \frac{K}{2} - B\left(\mu - \mu^*, \frac{K}{2}\right) \right\}, \quad (28)$$

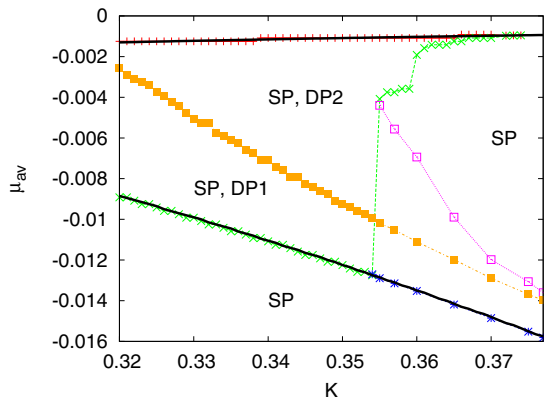


FIG. 10. Phase diagram near  $K = K_c \sim 0.355$  for the simplified oscillator model ( $\gamma = 0.02$ ,  $N = 4000$ ). Details are the same as in Fig. 2. The criteria to identify the boundaries are the same as in Fig. 9(b). The upper theoretical boundary (black curve) is drawn using Eq. (34).

where

$$B(s, w) \equiv \frac{\sqrt{s} \ln\{s + (1+w)^2\} - \ln\{s + (1-w)^2\}}{2 \tan^{-1}\left(\frac{1+w}{\sqrt{s}}\right) + \tan^{-1}\left(\frac{1-w}{\sqrt{s}}\right)}.$$

See the previous paper [26] for how to derive the last equation. The order parameter  $R$  is given by

$$R = \frac{\mu_{av} + \gamma - \mu^*}{2\gamma}. \quad (29)$$

As derived in Ref. [26], the critical value at which  $R$  vanishes turns out to be

$$\mu_c = -\gamma - \frac{K^2}{4} + \frac{2}{3}K\sqrt{2\gamma}. \quad (30)$$

The equation of  $R$  is also derived from Eqs. (27)–(29) (see Eq. (9) of Ref. [26]), leading to the formula  $K_{oc} = \sqrt{2\gamma}$ . By calculating  $\langle x_j^2 \rangle$  and using the expression of  $\langle x_j \rangle$  given in Eq. (6) of the same paper, where the  $j$ th unit is supposed to be oscillating, we obtain

$$S^2 = \frac{1}{N} \sum_{k=1}^N \langle (x_k - \langle x_k \rangle)^2 \rangle = \frac{1}{2\gamma} \int_{\mu^*}^{\mu_{av}+\gamma} d\mu \left[ \mu^* - \mu + \frac{2}{T} - \frac{1}{4T^2} \times \left\{ \ln \left( \frac{\mu + 1 - K + KX}{\mu + 1 + K + KX} \right) \right\}^2 \right], \quad (31)$$

where  $T$  is the period of an oscillating unit, i.e.,

$$T = \frac{1}{\sqrt{\mu - \mu^*}} \left\{ \tan^{-1} \frac{1 - (K/2)}{\sqrt{\mu - \mu^*}} + \tan^{-1} \frac{1 + (K/2)}{\sqrt{\mu - \mu^*}} \right\}.$$

For the case  $\mu_{av} + \gamma < \mu^*$ , all units become asymptotically stationary, thus enabling us to obtain the following equation

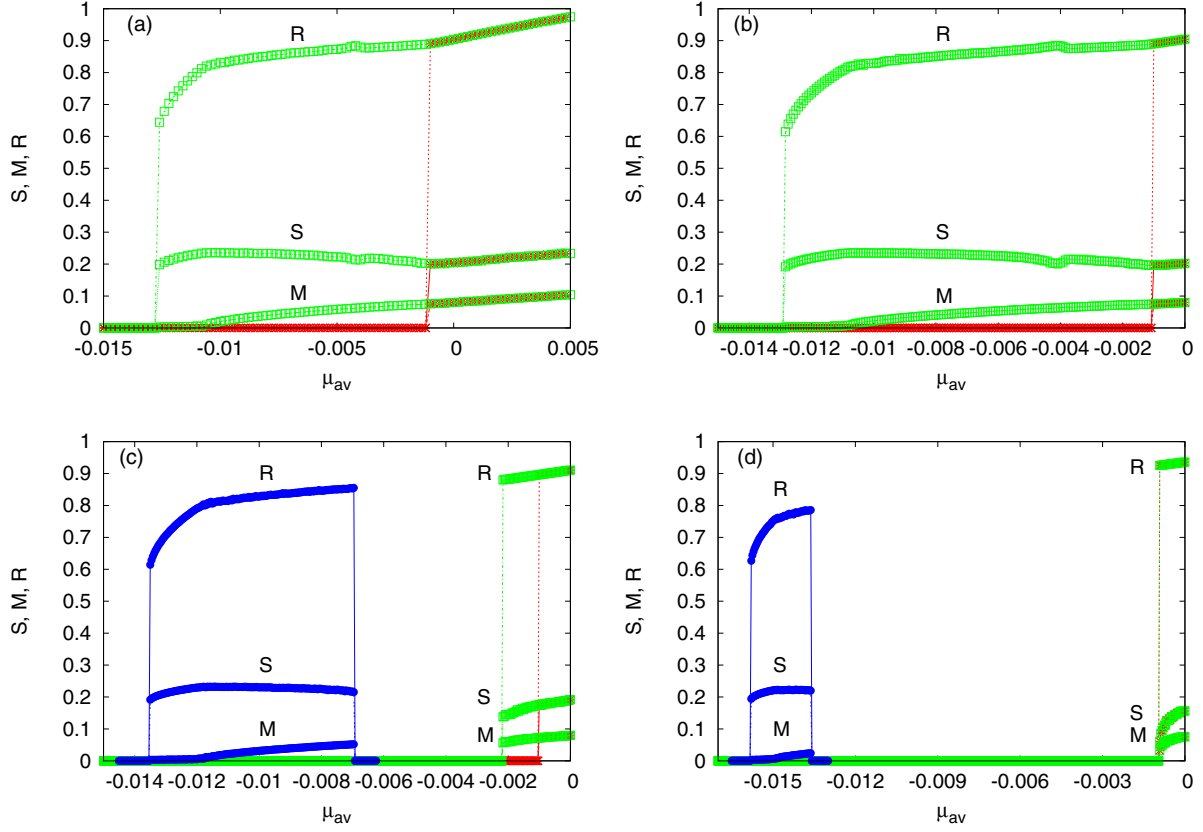


FIG. 11. Behaviors of the order parameters  $S$ ,  $M$ , and  $R$  in the simplified oscillator model ( $\gamma = 0.02$ ,  $N = 4000$ ). Relayed initial conditions are used (see the caption of Fig. 1). (a)  $K = 0.354$ ; (b)  $K = 0.354934$  (immediately before  $K = K_I$ ); (c)  $K = 0.36$  ( $< K_h \sim 0.374$ ); (d)  $K = 0.377$  ( $> K_h$ ). Other details are the same as in Fig. 3.

of  $X$ :

$$X = \frac{1}{2\gamma} \int_{\mu_{av}-\gamma}^{\mu_{av}+\gamma} d\mu \left( \frac{K}{2} - \sqrt{\mu^* - \mu} \right) \\ = \frac{K}{2} + \frac{1}{3\gamma} \left\{ (\mu^* - \mu_{av} - \gamma)^{\frac{3}{2}} - (\mu^* - \mu_{av} + \gamma)^{\frac{3}{2}} \right\}. \quad (32)$$

The remaining case is  $\mu_{av} - \gamma > \mu^*$ , in which case  $R = 1$  and we have the equation of  $X$  as follows:

$$X = \frac{1}{2\gamma} \int_{\mu_{av}-\gamma}^{\mu_{av}+\gamma} d\mu \left\{ \frac{K}{2} - B \left( \mu - \mu^*, \frac{K}{2} \right) \right\}. \quad (33)$$

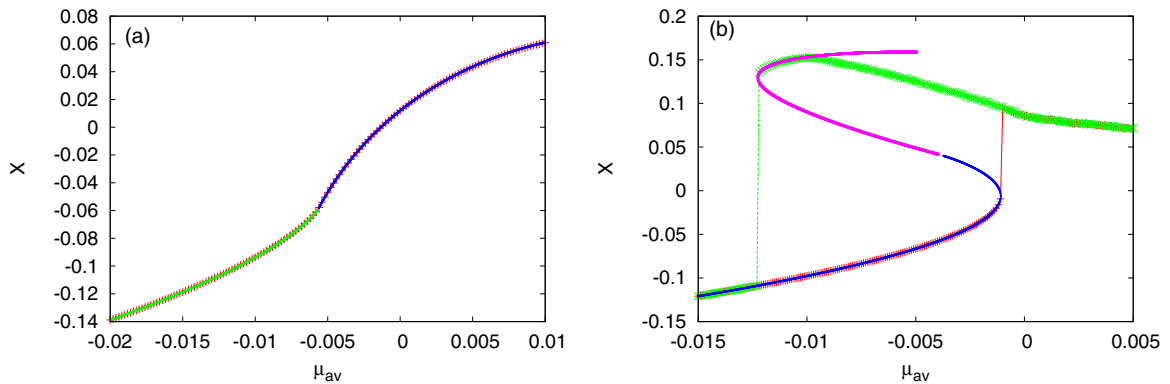


FIG. 12. Behavior of  $X$  in the simplified oscillator model ( $\gamma = 0.02$ ,  $N = 4000$ ). The simulation results here are time averages of  $X$ . (a)  $K = 0.15$  ( $< K_{oc} = 0.2$ ) (see the formula of  $K_{oc}$  in the text and Ref. [26]). The simulation results (+, red) exist in the whole region of  $\mu_{av}$ , which are perfectly covered by the theoretical results that consist of two parts:  $\mu_{av} < \mu_C \sim -0.005$ , where  $R = 0$  (SP, green curve), and  $\mu_{av} > \mu_C$ , where  $R > 0$  (DP1, blue curve). (b)  $K = 0.35$ . The branches connected with the two vertical lines are the simulation results which have been obtained by increasing (+, red) and decreasing ( $\times$ , green)  $\mu_{av}$  with relayed initial conditions (see the caption of Fig. 1). There are also two theoretical branches: Part of the lower branch (SP,  $R = 0$ , blue curve) with positive slopes perfectly overlaps with the simulation result, while the upper branch (DP1,  $R > 0$ , magenta curve) initially agrees with the branch obtained by simulation ( $\times$ , green), but starts to disagree after that, which is because the system enters DP2 there.

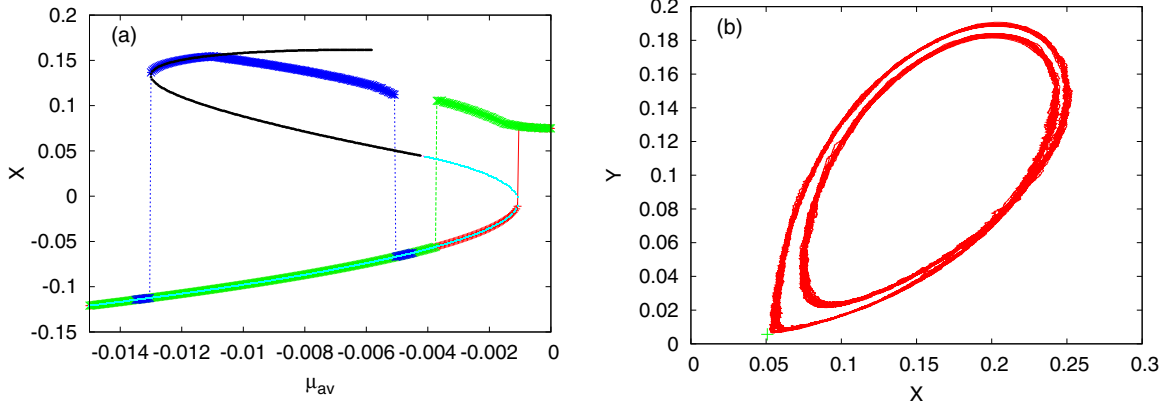


FIG. 13. Bifurcation diagram and trajectories in the simplified oscillator model ( $\gamma = 0.02$ ,  $K = 0.356 > K_c$ ). Simulation results ( $N = 4000$ ) have been obtained using relayed initial conditions (see the caption of Fig. 1). (a) Simulation results, which are time averages of  $X$ : data for increasing  $\mu_{av}$  (+, red) and for decreasing  $\mu_{av}$  ( $\times$ , green) and the floating branch with its neighborhoods included (asterisks, blue). The curves are based on theory: The upper black and lower cyan curves respectively correspond to DP1 and SP. The discontinuous transitions from DP2 to SP happen at  $\mu_{av} \sim -0.00506$  and  $\sim -0.00373$ . (b) Trajectories on the  $(X, Y)$  plane, where  $\mu_{av} = -0.0051458333\dots$  and  $Y$  is defined as  $\sum_{j=1}^N x_j^2/N$ . The orbit (red) is due to simulation, while the point (+, green) corresponds to DP1 (unstable, theory). Calculations of  $Y$  in SP and DP1 are easily performed on the basis of the theory developed in the text (see the Appendix).

In Fig. 13 as well as Fig. 12, some results obtained by solving the above equations are presented, showing nice agreement with simulation results. Using Eq. (32), it is possible to obtain the coordinate of the turning point existing in the branch of  $X$  with  $R = 0$  [see Fig. 12(b)], say,  $\mu_J = \mu_J$ ,

$$\mu_J = -\frac{K^2}{4} - \gamma + \frac{K}{3\gamma} \left\{ (2\gamma + U^2)^{\frac{3}{2}} - U^3 \right\} - U^2, \quad (34)$$

where  $U \equiv (K/2) - (\gamma/K)$ . This result reveals that  $\mu_J = \mu_c$  for  $K = K_{oc}$  and also that  $\mu_J > \mu_c$  for  $K > K_{oc}$ , in agreement with the simulation result displayed in Fig. 12(b). It should be noted that  $\mu_{av} = \mu_J$  corresponds to the boundary between SP and DP as  $\mu_{av}$  is increased from below in the region  $K > K_{oc}$  [see Figs. 9(b) and 10].

#### IV. SCALING BEHAVIORS OF ORDER PARAMETERS

Before concluding this paper, we here focus on how the order parameters  $S$  and  $M$  scale at the aging transition

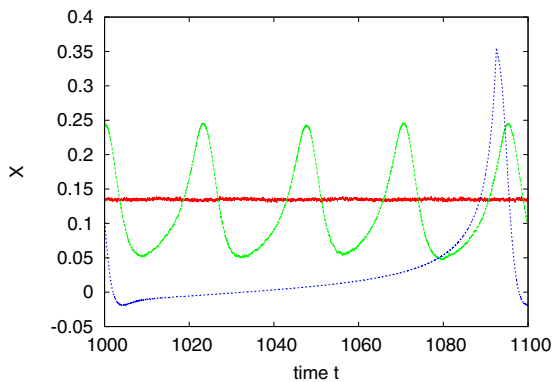


FIG. 14. Time series of  $X$  in the simplified oscillator model ( $\gamma = 0.02$ ,  $N = 4000$ ). The smallest (red), middle (green), and largest (blue) amplitude curves are the data for  $(K, \mu_{av}) = (0.3, -0.001)$ ,  $(0.33, -0.0005)$ , and  $(0.377, -0.0005)$ , respectively.

boundary. The main result is that their scaling laws vary from one region of  $K$  to another.

##### A. The case $0 \leq K < K_{oc}$

The previous paper [26] shows that in this case,  $R$  grows linearly from the critical point. This is done both analytically and numerically for the simplified model, while for the phase-oscillator model it is done only numerically, since analytical studies of the critical region is much harder in the latter. In this article, the same policy is taken again. In this region of  $K$ , the supercritical side belongs to DP1, where  $R > 0$  and  $M = 0$ , and hence we only have to focus on the critical behavior of  $S$  here. For a theoretical study, we employ the expression of  $S$  for the simplified model, as displayed in Eq. (31), which yields

$$S^2 = \frac{4}{3\pi} \sqrt{2\gamma} R^{\frac{3}{2}} + O(R^2), \quad (35)$$

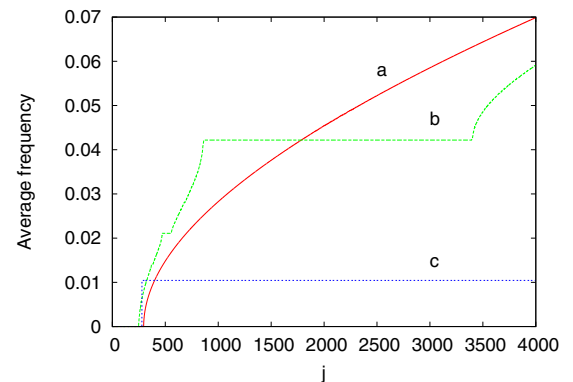


FIG. 15. Average frequency vs  $j$  for the simplified oscillator model ( $\gamma = 0.02$ ,  $N = 4000$ ). The parameters  $K$  and  $\mu_{av}$  of the data labeled “a”, “b”, and “c” are the same as those of the smallest, middle, and largest amplitude curves in Fig. 14, respectively.

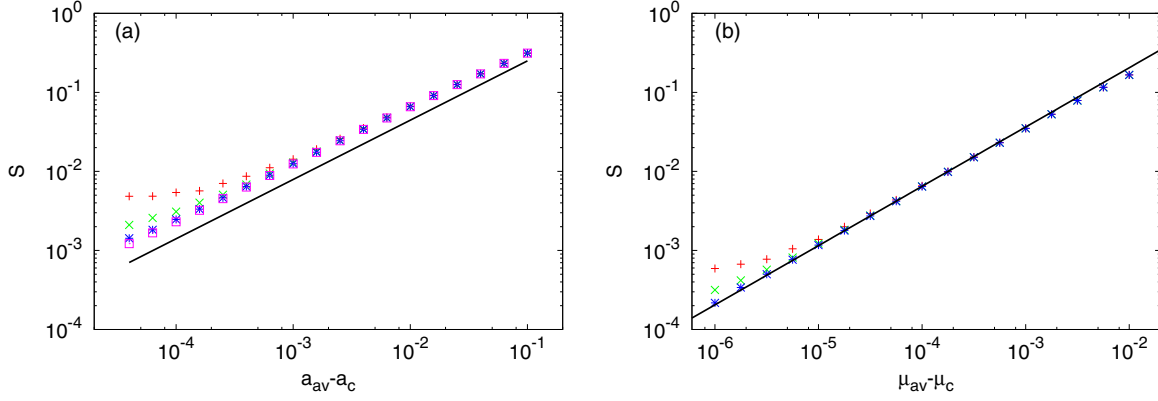


FIG. 16. Critical scaling behavior of  $S$  in the region  $0 \leq K < K_{oc}$ . The straight line in each panel shows the slope of  $3/4$ . (a) The phase-oscillator model with  $\gamma = 0.5$  and  $K = 0.5$ . The system size  $N$ : 1600 (+, red), 6400 ( $\times$ , green), 25 600 (asterisks, blue), 102 400 (squares, magenta). (b) The simplified oscillator model with  $\gamma = 0.02$  and  $K = 0.12$ . The system size  $N$ : 4000 (+, red), 16 000 ( $\times$ , green), 64 000 (asterisks, blue). The straight line here is drawn using the asymptotic formula of  $S$ , namely, Eq. (36) combined with Eq. (10) of Ref. [26].

as  $\mu_{av}$  approaches  $\mu_c$  from above. This result leads to the following relation between  $S$  and  $R$ :

$$S \cong \sqrt{\frac{4}{3\pi}} \sqrt{2\gamma} R^{\frac{3}{4}}. \quad (36)$$

Note that this relation holds for  $K = K_{oc}$  as well. Referring to  $R$ 's critical behavior in this region of  $K$  [26], we find that  $S$  obeys the following scaling law:

$$S \propto (\mu_{av} - \mu_c)^{\frac{3}{4}}. \quad (37)$$

This prediction is verified in Fig. 16 for both models.

### B. The case $K = K_{oc}$

It is shown in the previous paper [26] that the order parameter  $R$  grows with the exponent of  $2/3$  at  $K = K_{oc}$  for the two models. Combining this result with Eq. (36), we obtain

$$S \propto (\mu_{av} - \mu_c)^{\frac{1}{2}}. \quad (38)$$

The data presented in Fig. 17 support the above result for both models.

### C. The case $K = K_h$

Until the coupling strength  $K$  reaches  $K_h$  starting from  $K_{oc}$ , the transition to the dynamic phase remains discontinuous. Here we examine how the order parameters  $S$  and  $M$  scale at the aging transition boundary for  $K = K_h$ . Note that  $R$  itself makes an abrupt change from zero to a finite value for  $K > K_{oc}$ , irrespective of whether the transition is continuous or not (see Figs. 3 and 11). Since in the present case the mean-field is not constant in the supercritical region that lies in DP2, the self-consistent theory developed in the previous section is not applicable and also so for  $K > K_h$ . Hence, we need to rely on simulation results to clarify the critical behaviors of  $S$  and  $M$ . Figure 18 provides them for the two models, suggesting the scaling laws

$$S \propto (a_{av} - a_c)^{\frac{1}{5}}, \quad M \propto (a_{av} - a_c)^{\frac{1}{5}}, \quad (39)$$

for the phase-oscillator model and likewise for the simplified oscillator model. This unusual exponent of  $1/5$  may originate from the fact that for  $K = K_h$ , the saddle-node bifurcation of fixed points belonging to SP (SP) and the collision of the orbit

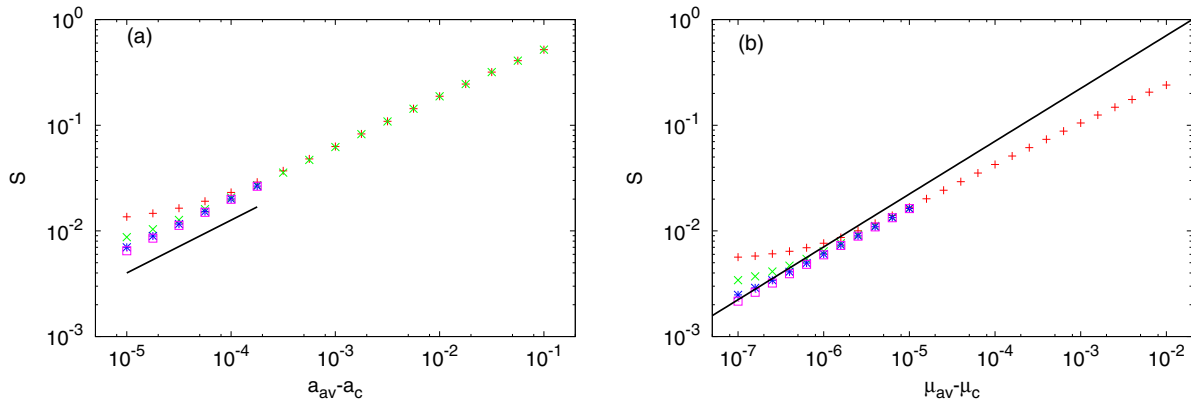


FIG. 17. Critical scaling behavior of  $S$  at  $K = K_{oc}$ . The straight line in each panel shows the slope of  $1/2$ . (a) The phase-oscillator model with  $\gamma = 0.5$ . The system size  $N$ : 4000 (+, red), 16 000 ( $\times$ , green), 64 000 (asterisks, blue), and 256 000 (squares, magenta). (b) The simplified oscillator model with  $\gamma = 0.02$ . The system size  $N$ : 8000 (+, red), 32 000 ( $\times$ , green), 128 000 (asterisks, blue), and 512 000 (squares, magenta). The straight line here is drawn in the same way as in Fig. 16(b).

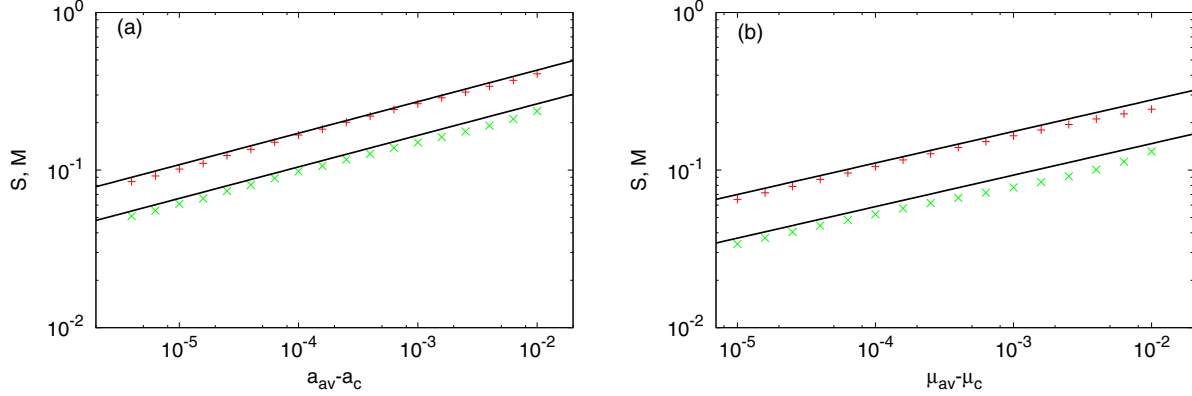


FIG. 18. Critical scaling behaviors of  $S$  and  $M$  at  $K = K_h$ . The symbols:  $S$  (+, red) and  $M$  ( $\times$ , green). The straight lines in each panel show the slope of  $1/5$ . (a) The phase-oscillator model with  $\gamma = 0.5$  and  $N = 25\,600$ . Here  $K = K_h = 1.156\,275$ . (b) The simplified oscillator model with  $\gamma = 0.02$  and  $N = 16\,000$ . In this case,  $K = K_h = 0.37\,375$ .

of  $Z$  ( $X, Y$ ; see the caption of Fig. 13 and Appendix for the definition of  $Y$ ) with the unstable fixed point occur at the same value of  $a_{av}$  ( $\mu_{av}$ ) in the phase (simplified) oscillator model. However, since no evolution equation of the mean field is available for each model at the moment, it remains as a future subject to derive the exponent theoretically.

#### D. The case $K > K_h$

Figure 19 displays an example of the critical behaviors of  $S$  and  $M$  for  $K > K_h$  for each model, suggesting the scaling laws

$$S \propto (a_{av} - a_c)^{\frac{1}{4}}, \quad M \propto (a_{av} - a_c)^{\frac{1}{4}}, \quad (40)$$

for the phase-oscillator model and likewise for the simplified oscillator model. As mentioned above, this region of  $K$  is out of the range where the self-consistent theory is applicable. A possible explanation is that the scaling laws in the present region of strong coupling may inherit those of  $S$  and  $M$  in the limit  $K \rightarrow \infty$ . Take the phase-oscillator model as an example. As discussed in Ref. [12], in this limit, all units are perfectly synchronized. Let the common phase be  $\theta$  and it obeys

$$\frac{d\theta}{dt} = a - \sin \theta, \quad (41)$$

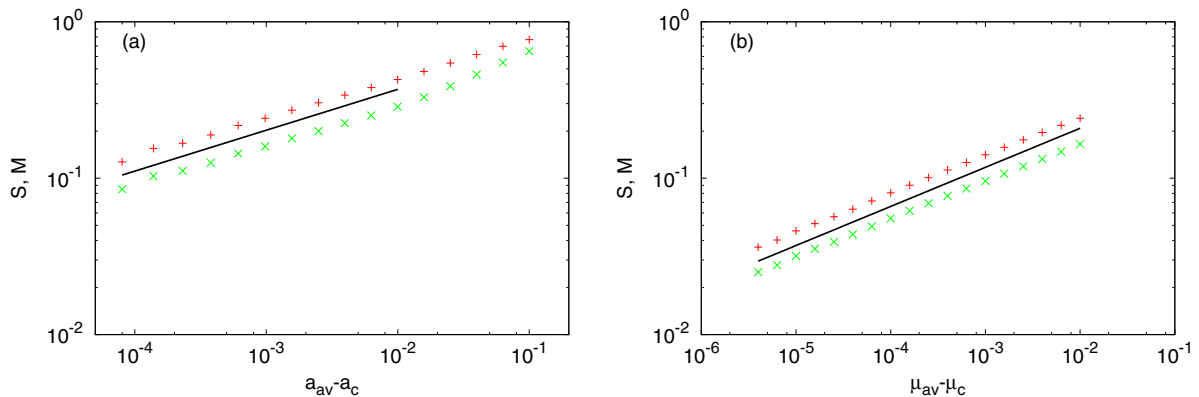


FIG. 19. Critical scaling behaviors of  $S$  and  $M$  for  $K > K_h$ . The symbols:  $S$  (+, red) and  $M$  ( $\times$ , green). The straight line in each panel shows the slope of  $1/4$ . (a) The phase-oscillator model with  $\gamma = 0.5$ ,  $K = 1.19$ , and  $N = 12\,800$ . (b) The simplified oscillator model with  $\gamma = 0.02$ ,  $K = 0.5$ , and  $N = 16\,000$ .

where  $a$  is used to stand for  $a_{av}$  for simplicity. In this limit,  $S$  equals  $M$  because of  $Z = e^{i\theta}$ . Some calculations enable us to obtain

$$\begin{aligned} S &= \sqrt{\langle |e^{i\theta} - \langle e^{i\theta} \rangle|^2 \rangle} \\ &= \sqrt{\frac{2}{a + \sqrt{a^2 - 1}}} (a^2 - 1)^{\frac{1}{4}} \\ &\cong 2^{\frac{3}{4}} (a - 1)^{\frac{1}{4}}, \end{aligned} \quad (42)$$

where the last expression is the one for the limit  $a \rightarrow 1 + 0$  (note that  $a_c \rightarrow 1$  for  $K \rightarrow \infty$  [12]). This result indicates that  $1/4$  is exactly the common scaling exponent of  $S$  and  $M$  in the strong coupling limit. Actually, numerical observations for finite  $K$  may explain  $M$ 's exponent. Figure 20 shows that the continuous transition from SP to DP2 for  $K > K_h$  seems to follow the SNIC scenario, namely, a limit cycle orbit emerges after the disappearance of a pair of stable and unstable fixed points that correspond to SP [see Fig. 20(a)]. In this case, the period of the limit cycle diverges, obeying an inverse square-root law as the control parameter approaches the saddle-node bifurcation point from above, which is consistent with the long period of  $Z$  as shown in Fig. 20(b). Hence, the above analysis performed for system (41) may be used to explain

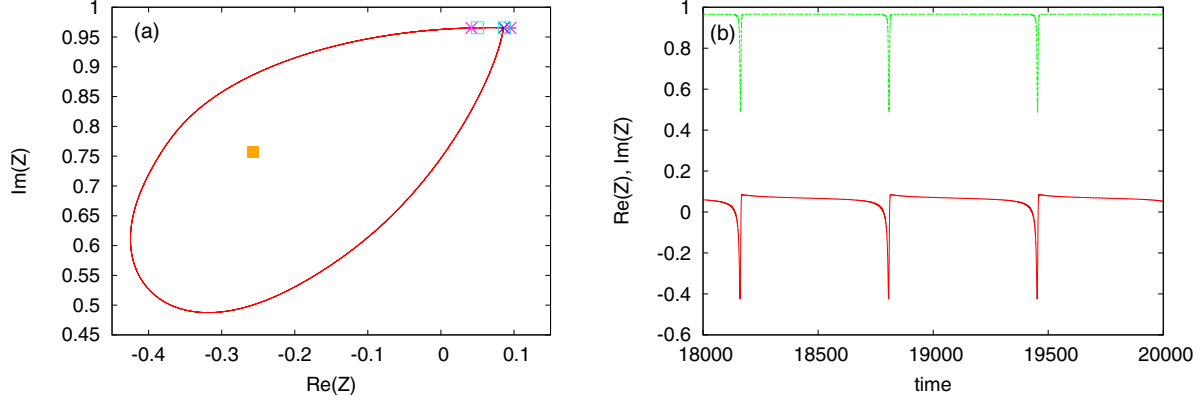


FIG. 20. Behavior of  $Z$  for  $K$  beyond and near  $K_h$  in the phase-oscillator model ( $\gamma = 0.5$ ,  $N = 6400$ ,  $K = 1.16 > K_h$ ). (a) A trajectory and fixed points on the complex plane. Simulation results: the orbit (red,  $a_{av} = 0.96575$ ), stable SP points; (+, green,  $a_{av} = 0.96525$ ) and ( $\times$ , blue,  $a_{av} = 0.9655$ ). Note that the latter SP points overlap SP points obtained by theory for the same parameter values (see below). Theory: two pairs of SP points (asterisks, magenta,  $a_{av} = 0.96525$ ; squares, cyan,  $a_{av} = 0.9655$ ), where in each pair, the left (right) one is unstable (stable), and the other is an unstable DP1 point (solid square, orange,  $a_{av} = 0.96575$ ). The validity of theory is confirmed by the excellent agreement between its SP points and corresponding simulation results. (b) Time series of  $\text{Re}Z$  (lower curve, red) and  $\text{Im}Z$  (upper curve, green), where the same data as the closed orbit in panel (a) are used ( $a_{av} = 0.96575$ ).

$M$ 's exponent,  $1/4$ , for  $K > K_h$ . However, the exponent of  $S$  is not explained at this stage.

## V. SUMMARY AND DISCUSSION

The present paper has clarified how transitions between the static and the dynamic phases occur for two models of globally coupled excitable and oscillatory units numerically and in part analytically. The distribution of bifurcation parameters is set to be the uniform type for each model. Common features of the two models are as follows: (1) a hysteresis region exists in the range  $K_{oc} < K < K_h$ ; (2) a floating branch starts from  $K = K_f$  at which the hysteresis loop drastically shrinks, which has been found to be caused by a collision between the mean-field's orbit and an unstable fixed point; (3) order parameter  $S$  exhibits different critical behaviors depending on  $K$ , i.e.,  $0 \leq K < K_{oc}$ ,  $K = K_{oc}$ ,  $K = K_h$ , and  $K > K_h$ ; and finally (4) order parameter  $M$  obeys the same scaling laws as  $S$  for  $K \geq K_h$ . To be more specific with (3), the critical exponent of  $S$ , say,  $\beta$ , decreases discontinuously as  $K$  grows, except for  $K = K_h$ :  $\beta = 3/4$  ( $K < K_{oc}$ ),  $1/2$  ( $K = K_{oc}$ ),  $1/5$  ( $K = K_h$ ),  $1/4$  ( $K > K_h$ ). In other words, the growth of  $S$  from zero tends to be sharper and sharper as the system proceeds to a larger  $K$  region.

In various applications of coupled oscillators, such as CPGs [22,23] and information processing (see, e.g., [33]), it is of vital importance to keep the dynamic activity of such systems against the deterioration of constituent oscillators caused by accidents or aging in the ordinary sense. Sufficient knowledge about the location of the aging transition boundary in the phase diagram and its structure would greatly help in avoiding the inactivation of the full system by controlling both the coupling strength and the average of bifurcation parameters (e.g., the average of external currents in neural populations). For this purpose, the above results should be quite useful. The branching of dynamic solutions (DP2) reported in the present paper produces a sharp decrease in the size of the hysteresis loop as the average value of bifurcation parameters is varied. The

magnitude of the sudden decrease is not large in each model, which is due to the small values of  $\gamma$  adopted in the present study. That magnitude increases by setting  $\gamma$  to be larger values [34] and also depends on the choice of a model from among a variety of candidates. This may also be the case with the size of the bistable region in the phase diagram. The knowledge of the branching, hysteresis, and bistability in between the small and large  $K$  regions can therefore be crucial information to evade a sudden inactivation of the whole system brought about by adjusting the coupling strength. It is also helpful in controlling the system that the critical scaling of  $S$  tells whether the supercritical side is DP1 or DP2. As to the generality of these findings, the simplified oscillator model taken up in the present work is composed of normal forms of the saddle-node bifurcation, as mentioned earlier. The fact that the model shows the above features may guarantee their generality. Our analysis has also provided with a possible scenario for the slowing of EEG [24] as stated at the beginning of this paper; i.e., it may be caused by the elongation of the period of the mean field as the system located in DP2 approaches the aging transition boundary in the course of ordinary aging, where the coupling strength needs to be larger than  $K_f$ .

However, there are some remaining subjects. First, at this stage, no accurate theory is available for the region DP2 where the mean field persistently oscillates, making it difficult to develop an exact theory. For this reason, the scaling laws of  $S$  and  $M$  found numerically for  $K \geq K_h$  are conjectures at this moment, although heuristic explanations have been given. For the same reason, the mechanism of the appearance of the floating branch is only based on numerical observations and part of the theoretical results. Second, the dimensionality of the units considered in the present study is unity and it remains unclear whether the above results hold when the unit dimensionality is greater than 1. In fact, the previous paper [26] reports that the way in which bistability starts to appear as the coupling strength exceeds a critical value depends on the unit dimensionality, i.e., a large population of globally coupled Morris-Lecar systems exhibits a different scenario in

this regard than the two models studied there and in this paper. Hence, more realistic models comprising higher-dimensional units need to be investigated to confirm to what extent the above features are general. These subjects are now under study and will be reported elsewhere.

#### ACKNOWLEDGMENT

This work was supported by KAKENHI (Grant-in-aid from the Japan Society for the Promotion of Science) Grant No. 26400401.

#### APPENDIX

Here presented are expressions of  $Y$  defined by

$$Y = \frac{1}{N} \sum_{j=1}^N x_j^2 \quad (\text{A1})$$

for SP and DP1 in the simplified oscillator model.

For SP,  $Y$  is given by

$$Y = \frac{K^2}{4} + \mu^* - \mu_{av} + \frac{K}{3\gamma} \{(\mu^* - \mu_{av} - \gamma)^{\frac{3}{2}} - (\mu^* - \mu_{av} + \gamma)^{\frac{3}{2}}\}, \quad (\text{A2})$$

where  $\mu^*$  is defined in Eq. (27). Then, for DP1,  $Y$  becomes

$$Y = \frac{1}{N} \sum_{j=1}^N \langle x_j^2 \rangle = Y_1 + Y_2 + \frac{1}{2\gamma} \int_{\mu^*}^{\mu_{av} + \gamma} d\mu \left\{ \frac{2}{T} + \frac{K}{2T} \ln \left( \frac{\mu + 1 - K + KX}{\mu + 1 + K + KX} \right) \right\}, \quad (\text{A3})$$

where the expression of  $T$  is given below Eq. (31) in the text, and

$$Y_1 \equiv \frac{K^2}{8\gamma} V - \frac{K}{3\gamma} V^{\frac{3}{2}} + \frac{1}{4\gamma} V^2, \quad (\text{A4})$$

with  $V \equiv \mu^* - \mu_{av} + \gamma$ , and

$$Y_2 \equiv \frac{1}{2\gamma} \left( \frac{K^2}{2} - KX \right) (\mu_{av} + \gamma - \mu^*) - \frac{1}{4\gamma} \{(\mu_{av} + \gamma)^2 - (\mu^*)^2\}. \quad (\text{A5})$$

- 
- [1] A. T. Winfree, *J. Theor. Biol.* **16**, 15 (1967).  
[2] A. T. Winfree, *The Geometry of Biological Time* (Springer, New York, 2001).  
[3] Y. Kuramoto, *Chemical Oscillations, Waves, and Turbulence* (Springer, Berlin, 1984).  
[4] A. Pikovsky, M. Rosenblum, and J. Kurths, *Synchronization—A Universal Concept in Nonlinear Sciences* (Cambridge University Press, Cambridge, UK, 2001).  
[5] S. H. Strogatz, *Phys. D (Amsterdam, Neth.)* **143**, 1 (2000).  
[6] J. A. Acebrón, L. L. Bonilla, C. J. P. Vicente, F. Ritort, and R. Spigler, *Rev. Mod. Phys.* **77**, 137 (2005).  
[7] I. Z. Kiss, Y. Zhai, and J. L. Hudson, *Science* **296**, 1676 (2002).  
[8] H. Daido and K. Nakanishi, *Phys. Rev. Lett.* **93**, 104101 (2004).  
[9] H. Daido and K. Nakanishi, *Phys. Rev. E* **75**, 056206 (2007); **76**, 049901(E) (2007).  
[10] H. Daido, *Europhys. Lett.* **84**, 10002 (2008).  
[11] H. Daido, *Phys. Rev. E* **83**, 026209 (2011).  
[12] H. Daido, *Phys. Rev. E* **84**, 016215 (2011).  
[13] H. Daido, *AIP Conf. Proc.* **1468**, 127 (2012).  
[14] D. Pazó and E. Montbrio, *Phys. Rev. E* **73**, 055202(R) (2006).  
[15] G. Tanaka, Y. Okada, and K. Aihara, *Phys. Rev. E* **82**, 035202(R) (2010).  
[16] K. Morino, G. Tanaka, and K. Aihara, *Phys. Rev. E* **83**, 056208 (2011).  
[17] B. Thakur, D. Sharma, and A. Sen, *Phys. Rev. E* **90**, 042904 (2014).  
[18] G. Tanaka, K. Morino, and K. Aihara, *Sci. Rep.* **2**, 232 (2012).  
[19] G. Tanaka, K. Morino, H. Daido, and K. Aihara, *Phys. Rev. E* **89**, 052906 (2014).  
[20] W. Huang, X. Zhang, X. Hu, Y. Zou, Z. Liu, and S. Guan, *Chaos* **24**, 023122 (2014).  
[21] J. Miake, E. Marbán, and H. B. Nuss, *Nature (London)* **419**, 132 (2002).  
[22] J. D. Murray, *Mathematical Biology* (Springer, Berlin, 1993).  
[23] A. J. Ijspeert, A. Crespi, D. Ryczko, and J.-M. Cabelguen, *Science* **315**, 1416 (2007).  
[24] N. Benz, F. Hatz, H. Bousleiman, M. Ehrensperger, U. Gschwandtner, M. Hardmeier, S. Ruegg, C. Schindler, R. Zimmermann, A. Monsch, and P. Fuhr, *Front. Aging Neurosci.* **6**, 314 (2014).  
[25] P. Fries, *Neuron* **88**, 220 (2015).  
[26] H. Daido, A. Kasama, and K. Nishio, *Phys. Rev. E* **88**, 052907 (2013).  
[27] C. Morris and H. Lecar, *Biophys. J.* **35**, 193 (1981).  
[28] The first model of this kind would be the one studied in S. Shinomoto and Y. Kuramoto, *Prog. Theor. Phys.* **75**, 1105 (1986). Since then, a number of studies have been made on similar models for different purposes than the present subject, except for Refs. [12,14,26]. Some examples are referred to in Ref. [26].  
[29] Model (3) is motivated by the simplest model of neurons known as the Peskin model [C. S. Peskin, in *Mathematical Aspects of Heart Physiology* (Courant Institute of Mathematical Sciences, New York University, New York, 1975)], in which the only variable of each unit makes a discontinuous transition to zero when it reaches unity, i.e., the unit fires. The Peskin model is pulse coupled and easily simulated by an event-driven method because there is no interaction while all units are evolving without firing. However, in our model (3) each unit always

interacts with all the others, so the event-driven method is not applicable. This is the reason why we have performed numerical simulations as just described in the text. Since the time step 0.01 is so small, simulation results agree with theory, as demonstrated in the text.

- [30] D. Golomb and J. Rinzel, *Phys. Rev. E* **48**, 4810 (1993).  
 [31] A. Pikovsky, M. Rosenblum, and J. Kurths, *Europhys. Lett.* **34**, 165 (1996).  
 [32] G. Nicolis, *Introduction to Nonlinear Science* (Cambridge University Press, Cambridge, UK, 1995).

- [33] H. Sompolinsky, D. Golomb, and D. Kleinfeld, *Proc. Natl. Acad. Sci. USA* **87**, 7200 (1990).  
 [34] For the simplified oscillator model, it is possible to obtain using Eqs. (30) and (34)

$$\mu_J - \mu_C = \frac{\gamma}{6} \Phi\left(\frac{K - K_{oc}}{K_{oc}}\right),$$

with  $\Phi(x) \equiv 3x^2 - 2x + 1 - 1/(x + 1)^2$ , where the region  $K \geq K_{oc}$  is considered. This result might imply that the size of the hysteresis loop and the magnitude of its sudden decrease is of the order  $\gamma$ .